Research Article

Nano Research
2022, 15(4): 3246–3253

ISSN 1998-0124 CN 11-5974/O4
https://doi.org/10.1007/s12274-021-3968-9

# A humidity resistant and high performance triboelectric nanogenerator enabled by vortex-induced vibration for scavenging wind energy

Yan Wang[1,2,§], Tianyu Chen[1,§], Shuowen Sun[1,§], Xiangyu Liu[1], Zhiyuan Hu[1], Zhenhui Lian[1], Long Liu[2], Qiongfeng Shi[2], Hao Wang[2], Jianchun Mi[3], Tongming Zhou[4] (✉), Chengkuo Lee[2] (✉), and Minyi Xu[1] (✉)

[1] *Dalian Key Lab of Marine Micro/Nano Energy and Self-powered System, Marine Engineering College, Dalian Maritime University, Dalian 116026, China*
[2] *Center for Intelligent Sensors and MEMS (CISM), National University of Singapore, 4 Engineering Drive 3, Singapore 117576, Singapore*
[3] *College of Engineering, Peking University, Beijing 100871, China*
[4] *School of Civil, Environmental and Mining Engineering, The University of Western Australia, WA 6009, Australia*
[§] *Yan Wang, Tianyu Chen, and Shuowen Sun contributed equally to this work.*


**Received:** 30 September 2021 / **Revised:** 23 October 2021 / **Accepted:** 31 October 2021

## ABSTRACT

Wind energy is a promising renewable energy source for a low-carbon society. This study is to develop a fully packaged vortex-induced vibration triboelectric nanogenerator (VIV-TENG) for scavenging wind energy. The VIV-TENG consists of a wind vane, internal power generation unit, an external frame, four springs, a square cylinder and a circular turntable. The internal power generation unit consists of polytetrafluoroethylene (PTFE) balls, a honeycomb frame and two copper electrodes. Different from most of the previous wind energy harvesting TENGs, the bouncing PTFE balls are fully packaged in the square cylinder. The distinct design separates the process of contact electrification from the external environment, and at the same time avoids the frictional wear of the ordinary wind energy harvesting TENGs. The corresponding VIV parameters are investigated to evaluate their influence on the vibration behaviors and the energy output. Resonant state of the VIV-TENG corresponds to the high output performance from the VIV-TENG. The distinct, robust structure ensures the full-packaged VIV-TENG can harvest wind energy from arbitrary directions and even in undesirable weather conditions. The study proposes a novel TENG configuration for harvesting wind energy and the VIV-TENG proves promising powering micro-electro-mechanical appliances.

## KEYWORDS

vortex-induced vibration, wind energy, triboelectric nanogenerator, self-powered

## 1 Introduction

Converting the ambient energy to electricity has proved to be an effective method for powering micro-electro-mechanical systems [1–11], such as sensors and actuators. As wind is virtually an enormous, carbon-free energy, it is an ideal energy source for self-powered system. Electromagnetic generators have been widely used for converting wind energy to electricity [12, 13]. However, conventional electromagnetic wind turbine is designed for large-scale grid power supply, which is not suitable for small mobile electronics, distributed sensors and sensing system (such designs make the whole device complicated, heavy, and costly). In this case, alternative wind energy harvesting method for powering distributed electrical appliances is highly desired.

Ascribing to the advantages such as low manufacturing cost [14–17], easy fabrication [18–20] and good scalability [21–23], triboelectric nanogenerator (TENG) with different structures have demonstrated considerable abilities to harvest wind energy. The flutter-driven and rotational structure based TENG have been considered as the effective wind energy harvesters [24–31]. However, its output performance could be substantially reduced by the relative humidity (RH) of the environment. Moreover, these TENGs are also subject to friction wear, rotational resistance and high wind speed in application domains. Therefore, researchers need to develop a TENG with sealed tribo-layer (from environmental disruptions), high durability and output performance.

The vortex-induced vibration (VIV) is a common physical phenomenon in fluid dynamics. It is induced by vortex shedding formed by the fluid passing around a bluff structure [32, 33]. The VIV can give rise to fatigue failure that undermines the structure service life. On the other hand, the large vibration amplitude implies much mechanical energy is captured by the structure. How to convert this kind of energy to electricity in an efficient way has drawn great attention in recent years. However, high stiffness and low cycle life makes the piezoelectric VIV wind energy harvester not suitable for applying in low wind speed and long-term operation conditions. Highly cost and complex structure makes the electromagnetic VIV wind energy harvester not suitable for application where low cost and maintenance-free are needed. A few TENG-based vibration energy harvesters and vibration

Address correspondence to Tongming Zhou, xuminyi@dlmu.edu.cn; Chengkuo Lee, elec@nus.edu.cn; Minyi Xu, xuminyi@dlmu.edu.cn

sensors have been developed and published [34, 35]. By combining VIV phenomenon with TENG structure, these studies have provided a solution to harvest fluid mechanical energy.

In this study, a fully packaged VIV triboelectric nanogenerator (VIV-TENG) is constructed to for harvest energy in a wind tunnel. It consists of four springs, a frame structure, a polylactic acid (PLA) square cylinder and a power generation unit. The power generation unit is comprised by PTFE balls, two copper electrodes and a honeycomb frame. When wind flows around the square cylinder, VIV occurs over a wide range of wind speed. The PTFE balls in the square cylinder bounce and contact with two copper electrodes repeatedly, producing alternating electrical signals. The wind tunnel experiments are conducted under different mass ratios to examine its effects on the synchronization region of the structure. The VIV-TENG has also been designed to harvest wind energy from arbitrary wind directions. More importantly, the presented VIV-TENG demonstrates a good output performance and durability even in high humidity condition due to its unique waterproof and solid structure design.

## 2 Results and discussion

### 2.1 Design and working mechanism of the VIV-TENG

As shown in Fig. 1(a), the VIV-TENG consists of four parts, i.e. a square cylinder as the vibrator, its internal power generation unit, 4 springs and an external frame. The square cylinder and internal frame are printed with PLA material and UV curable resin, respectively. The internal power generation unit is made of two copper electrodes, PTFE balls and a honeycomb frame. The experiments on the vibration and power generation performance are conducted in the wind tunnel as shown in Fig. 1(aiii). The VIV-TENG is fixed on the frame with four springs. When wind flows over it, a periodic vortex shedding forms in the wake at the rear of the VIV-TENG as depicted in Fig. 1(b). If the vortex shedding frequency $f_{vs}$ matches the natural frequency $f_n$ of the square cylinder, the latter starts to vibrate. This is considered as the vortex-induced vibration, and the range where VIV occurs is the lock-on region. Previous studies have shown that square cylinders yields the higher vibration amplitude and wider lock-on region than semi-circular and a circular cylinders [36]. Higher vibration amplitude results in higher acceleration which can deliver a higher electrical output.

The power generation mechanism is shown in Fig. 1(c). When the PTFE balls contact with the surface of the bottom electrode, PTFE balls attract electrons from copper. Therefore, the net positive charges distribute in copper electrode and the net negative charges distribute in the surface of the PTFE ball, respectively. As the square cylinder vibrates, the PTFE balls in the internal power generation unit starts to bounce with the oscillator. They get separated from the electrode at the bottom and moves upward. In this process, the electric potential difference between two electrodes drives the positive charges to flow through external circuit from the bottom electrode to the top. When the PTFE balls contact with the surface of the top electrode, positive charges on the bottom electrode transfer to the top one. As the PTFE ball moves in the opposite direction, a reversed current is generated in this process. Thus, the periodic alternating current can be generated in the external circuit. The corresponding electrostatic field distribution of the VIV-TENG is simulated by the COMSOL Multiphysics software. In the simulation, the distance between the two electrodes is set to be 8 mm and the diameter of the PTFE ball is set as 5 mm. The simulation result is demonstrated in Fig. S1 in the Electronic Supplementary Material (ESM).

According to the governing equation for the freestanding TENG [37], the VIV-TENG output voltage (V) can be described by

$$V = -\frac{1}{C}Q + V_{OC} = -\frac{d_0 + G}{\varepsilon_0 S}Q + \frac{2\sigma x}{\varepsilon_0} \quad (1)$$

where $Q$ and $V_{OC}$ represents the total transferred charge and open circuit voltage, respectively. $C$, $d_0$, $G$, and $S$ is the total capacitance, the dielectric material effective thickness, the air gap thickness between two copper electrodes, and the contacting area size, respectively; $\sigma$ denotes the charge density, $x$ denotes the distance between PTFE balls and electrodes, and $\varepsilon_0$ denotes the dielectric constant.

### 2.2 Vibration characteristics of the VIV-TENG

VIV is fundamentally a nonlinear phenomenon [32], in which the vibration of the structure is induced by vortex shedding. Meanwhile, the vibrating structure interacts with the flow field. For a VIV-TENG module, mild transverse oscillation can be also observed in the experiment, but the primary response mode is transverse to the wind. VIV is initiated as the vortex shedding frequency $f_{vs}$ matches the natural frequency $f_n$ of the cylinder [38]. With the increase of the wind speed $U$, the vibration amplitude of the cylinder increases rapidly with velocity, or which can be represented as the non-dimensional reduced velocity $U^*$.

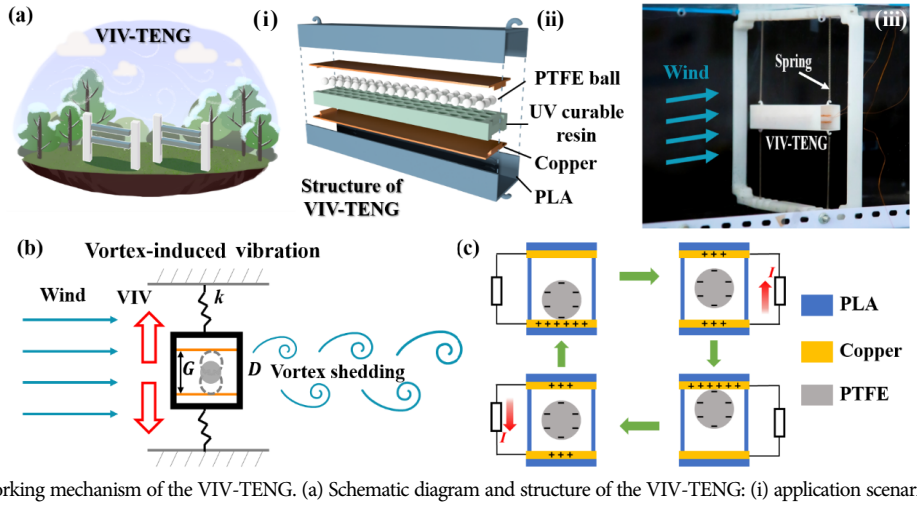


**Figure 1** Design and working mechanism of the VIV-TENG. (a) Schematic diagram and structure of the VIV-TENG: (i) application scenario of the VIV-TENG, (ii) detailed structure of the VIV TENG, (iii) experimental set up in the wind tunnel; (b) vortex-induced vibration of the VIV-TENG; (c) working principle of the VIV-TENG.

$$U^* = \frac{U}{f_n D} \tag{2}$$

where $D$ is the height of the square cylinder. The natural frequency of the VIV-TENG can be obtained from Eq. (3)

$$f_n = 2\pi\sqrt{\frac{k}{m_{osc}}} \tag{3}$$

here $k$ is the spring stiffness constant and $m_{osc}$ represents the oscillating mass (mass of the square cylinder). The mass of the cylinder ($m_{osc}$) and the number of PTFE ball ($n$) are determined by the dimension of the square cylinder. The number of PTFE ball is a key parameter to the output performance of the VIV-TENG. Previous studies [39, 40] showed that the VIV characteristics depend on the mass ratio $m^* = m_{osc}/m_d$, structural damping factor $\zeta$ and their product $m^*\zeta$ (mass-damping ratio). Where, $m_d = \rho V_1$ is the displaced air mass, $V_1$ is the displaced fluid volume and $\rho$ is the fluid density. Therefore, the dimension of the square cylinder can affect its vibration and power generation characteristics. In our work, different dimensions of the square cylinder are adopted. The mass of these cylinders is set to 54 g by adding mass block in the square cylinder to achieve the same $m_{osc}$. Different mass ratios VIV-TENG are tested in wind tunnel to achieve the vibration and power generation characteristics.

For a high mass ratio system ($m^* \geq 250$), synchronization (or lock in) will occur when the ratio $f^* = f_{vs}/f_n$ is close to 1.0 [38, 41]. The frequency of vortex shedding $f_{vs}$ is equal to the vibration frequency $f_v$ as the wake pattern of the VIV-TENG is classified as the two single mode (2S mode), in which two single vortices shed per cylinder oscillation cycle (during one period) [42]. As can be seen from the Movie ESM1, two single vortices are generated in a period of vibration. The measured vibration signals are analyzed with Fast Fourier Transform (FFT) to obtain the vibration frequency $f_v$. Images captured by the high-speed camera can also be used to reveal the vibration frequency.

As shown in Figs. 2(a) and 2(b), the clockwise and counter-clockwise vortices are presented clearly at the rear of the square cylinder. The amplitude and the vortex scale are much higher when $U^*$ increases from 7.02 to 40.26 as shown in Figs. 2(a) and 2(b) and Movie ESM2. The experimental results for three different mass ratios are presented and discussed to show its relevance to lock-in region and the vibration amplitude. Parameters of the square cylinder and the spring used in this work are listed in Table 1.

To improve the VIV-TENG energy extraction efficiency, a high vibration amplitude and a wide synchronization range is required [43]. Material damping $\zeta$ (determined in vacuum which is a constant) and nondimensional mass ratio (as the "mean mass density") are the key parameters determining the vibration amplitude and synchronization range in a VIV system [32]. According to Bernitsas et al. [43], the design process of the fluid energy harvester requires high vibration amplitude under high damping over a broad range of synchronization. In addition $\zeta$ can be obtained using $\zeta = (1/2\pi)\ln(y_{n+1}/y_n)$ from a free decay test [44].

Sarpkaya [42] showed that the mass damping ratio $\zeta m^*$ is the parameter controlling the peak amplitude of vibration. As shown

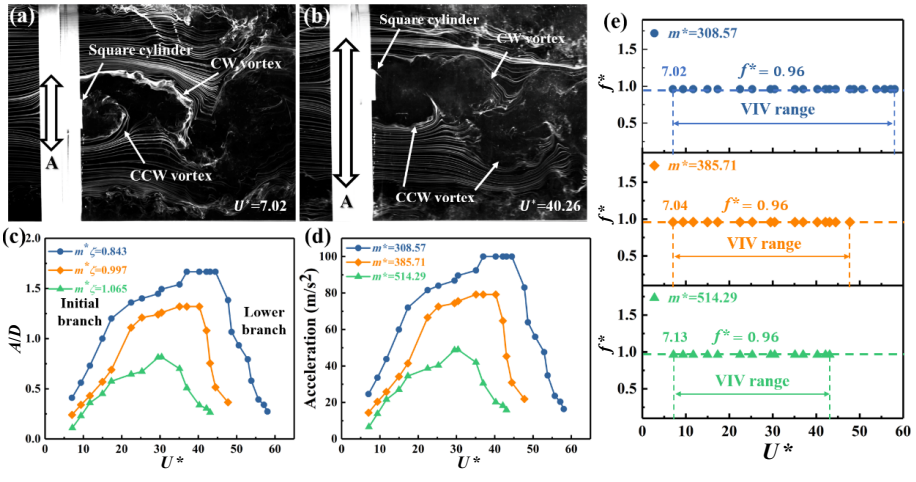


**Figure 2** Vortex-induced vibration characteristics. Visualization of fluid interaction with the square cylinder at (a) $U^* = 7.02$ and at (b) $U^* = 40.26$; (c) amplitude ratio ($A/D$) as a function of normalized velocity; (d) vibration acceleration as a function of normalized velocity; (e) nondimensional frequency of response ($f^*$) versus nondimensional velocity ($U^*$).

**Table 1** Experimental parameters

| Case | 1 | 2 | 3 |
|---|---|---|---|
| Spring stiffness (N/m) | 27 | 27 | 27 |
| Spring inner diameter (mm) | 2.58 | 2.58 | 2.58 |
| Spring out diameter (mm) | 3.06 | 3.06 | 3.06 |
| Spring length (mm) | 44.51 | 44.51 | 44.51 |
| Mass of the cylinder (g) | 54 | 54 | 54 |
| Length (mm) | 150 | 120 | 90 |
| Width (mm) | 30 | 30 | 30 |
| Height (mm) | 30 | 30 | 30 |
| Damping factor ($\zeta$) | 0.002733 | 0.002585 | 0.002071 |
| Mass ratio ($m^*$) | 308.57 | 385.71 | 514.29 |

in Fig. 2(c), decreasing $\zeta m^*$ can result in high vibration amplitude. It is apparent that for the high $m^*$ cases, two amplitude branches are involved in the vibrating process, namely, the initial and lower branches [40], which is consistent with the previous results [32, 43, 45]. For example, when $\zeta m^* = 0.843$, synchronization occurs at $U^*$ 7.02–58.05 (corresponding wind speed is 1.5–12.4 m/s) as shown in Fig. 2(c), which is much wider than that for circular cylinders vibrating in air [41] and the square cylinders in this work ($\zeta m^* = 0.997$ and $m^* = 1.065$).

The power generation of the VIV-TENG is determined by its acceleration [34]. The vibration of the square cylinder can be treated as harmonic vibration, which can be demonstrated as $Y = A\sin(\omega t + \varphi)$. $A$, $\omega$, $t$, $\varphi$ denotes the maximum vibration amplitude, angular velocity, transient time and initial phase angle, respectively. The vibration acceleration ($a$) and its maximum value ($a_m$) can be written as $a = -A\omega^2\sin(\omega t + \varphi)$ and $a_m = A(2\pi f_v)^2$ by differentiating Y. Figure 2(d) demonstrates the acceleration versus $U^*$ at the three different values of $m^*$. Evidently, the higher acceleration is resulted from a lower mass ratio. The lock-in or synchronization of the vibrating structure traditionally means that the ratio $f^*$ remains close to 1.0, i.e., $f_v \approx f_n$. In this study, $f^* = 0.96$ when the VIV-TENG is in the synchronization range. Khalak and Williamson [39] demonstrated that the range of synchronization is controlled primarily by $m^*$. Indeed, it is the case (as can be seen in Fig. 2(e)). When a lower mass ratio results in a larger synchronization range. Therefore, the VIV-TENG with $m^* = 308.57$ is expected to outperform in the three cases for harvesting wind energy, considering that it could deliver a larger amplitude, a larger synchronization range and a higher acceleration. In this sense, the VIV-TENG with $m^* = 308.57$ is tested for the evaluating the output performance of the VIV-TENG.

### 2.3 Output performance of the VIV-TENG

To investigate the dependence of VIV-TENG performance on the number of PTFE balls ($n$), electrical output signals of the VIV-TENG are measured for $n$ = 6 to 43 and shown in Figs. 3(b)–3(d). A square cylinder with a length of 150 mm is used as the vibrator to generate the electrical signal. Increasing 6 PTFE balls in the honeycomb structure each time can make the whole square cylinder balance all the time as shown in Fig. 3(a). It can keep the gravity center of the square cylinder at the balanced position all the time. The tested VIV-TENG with different $n$ is always kept the same $m_{osc}$ of 54 g (corresponding to $m^* = 308.57$). As depicted in Figs. 3(b)–3(d), the open circuit voltage, short circuit current and transferred charge increase with $n$. The maximum voltage, current and transferred charge can reach 107.14 V, 3.54 A and 36.91 nC when $n = 43$. More PTFE balls mean the large contact area between the dielectric material with the electrodes, the open-circuit voltage becomes higher, as well as the transferred charge. The voltage, current and transferred charge all increase roughly linearly with $n$ as shown in Fig. S2 in the ESM. Every PTFE ball corresponds to a TENG unit. 43 PTFE balls in power generation unit represents 43 TENG units connected in parallel. This might be contradictory, as voltage should have not increased when the units are connected in parallel. This is due to the actual voltage decreased with the increase of units. The explanation is demonstrated in Fig. S7 and Note S1 in the ESM. This indicates that higher output could be achieved by simply adding more PTFE balls, but it is not multiplied increase. For $n = 43$, the VIV-TENG average output power increases to 1.682 mW (corresponding to a power density of 62.2 W/m$^3$) when the matched loading resistance is 200 MΩ, see Fig. 3(e). The comparison of the output power for different $n$ indirectly approves that the power increases with the number of VIV-TENG units in parallel. The distance between two copper electrodes ($G$) is an important design parameter to affect output performance of VIV-TENG according to Eq. (1). Figure 3(f) and Fig. S3 in the ESM clearly demonstrate that the electrical output increases with $G$ at first and then decreases when $G >$ 8 mm. The decrease occurs because the PTFE ball can hardly contact with the top copper electrode when $G >$ 8 mm. This results in the decrease of the transferred charge between the PTFE ball and the electrode. Note that the experiments for different $G$ are conducted at the resonance state of the VIV-TENG, which corresponds to $U^*$ = 29.49.

The output performance of TENG can be substantially influenced by the surrounding environment, especially, under high relative humidity (RH) and high wind speed. If the water vapor exists on the PTFE ball and copper electrode, the triboelectric charges will reduce and even discharge [46]. As shown in Fig. 4(a), the humidity tests are conducted in the wind tunnel with $U^*$ = 40.26. As the internal power generation unit is totally sealed by the tape, the VIV-TENG has the humidity resistant characteristic that ensures it to work securely under high humidity conditions. Figure 4(b) displays the voltage signals under five different values of the relative humidity. Strikingly, no obvious difference is observed between the signals for RH = 60% and RH = 100%. For the VIV-TENG with $m^*$ =308.57, when $U^*$ >7.02 as

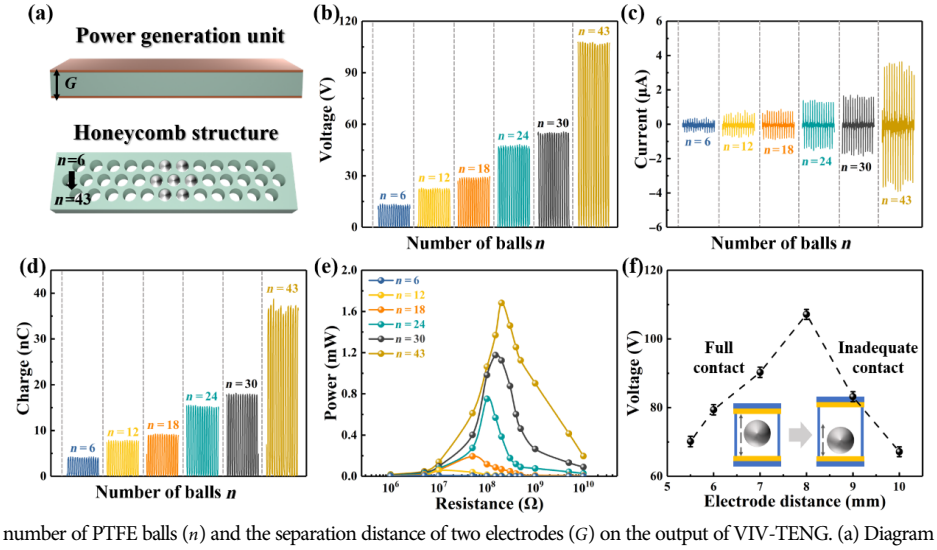


**Figure 3** Effects of the number of PTFE balls ($n$) and the separation distance of two electrodes ($G$) on the output of VIV-TENG. (a) Diagram of the power generation unit; (b)–(e) $n$-effect: (b) open circuit voltage, (c) short circuit current, (d) transferred charge, (e) output power; (f) output voltage for different $G$.

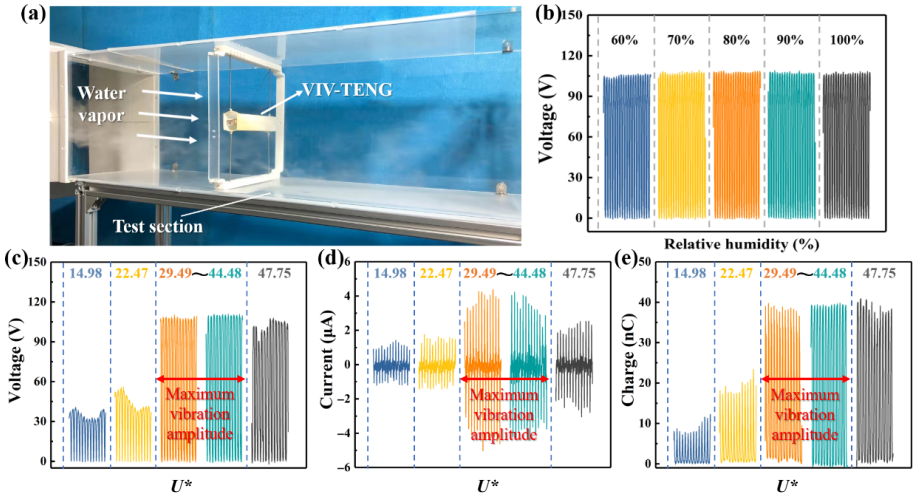


**Figure 4** (a) Schematic of the experimental setup; (b) dependence of the output voltage of the VIV-TENG on the relative humidity; dependence of the VIV-TENG power generation performance under different wind speeds. Effect of $U^*$: (c) Open circuit voltage; (d) short circuit current; (e) transferred charge of VIV-TENG.

shown in Fig. 2(c), the VIV-TENG starts to vibrate and delivers the electric signal. The outputs increase with $U^*$ until the wind speed enters the maximum vibration amplitude range ($U^*$ =24.49–44.98). In this range, the VIV-TENG can deliver the stable and maximum outputs of voltage, current and transferred charge, see Figs. 4(c)–4(e), which can reach 107.14 V, 3.54 A and 36.91 nC, respectively. The vibration amplitude and acceleration of the VIV-TENG with $m^* = 308.57$ increase in the initial branch and decrease in the lower branch as shown in Figs. 2(c) and 2(d). The vibration amplitude and acceleration increase until the reduced velocity reaches 29.49 with a corresponding amplitude 1.5D and acceleration 86.77 m/s$^2$, respectively. This indicates that once the acceleration exceeds 86.77 m/s$^2$, the transferred charge between the PTFE ball and two electrodes reaches maximum value. Meanwhile, the amplitude and acceleration also reach the maximum value. Thus, the VIV-TENG can deliver a stable and maximum output in the reduced velocity range of 29.49–44.98. As the wind speed increases to $U^* = 47.75$, the VIV enters the lower branch, and the amplitude of the VIV-TENG reduces. The output becomes unstable and decreases slightly.

Figure S4 shows that the output voltage is steady over 5,000 seconds at the relative humidity of 100%, confirming the excellent humidity resistance of the VIV-TENG. The electrical output performance is the key factor of the TENG. Table S1 in the ESM lists the power density of the present VIV-TENG versus those of other types of TENG based wind energy harvesters. Apparently, the present VIV-TENG does not perform very poorly. More importantly, it exhibits a lower critical velocity than those wind energy harvesters do. As shown in Table S2 in the ESM, some previous wind energy harvesters enabled by vortex-induced vibration are summarized. The performance of the present VIV-TENG is not inferior compared to the piezoelectric wind energy harvester enabled by vortex-induced vibration. Furthermore, the VIV-TENG is more durable than those cantilever beam design.

### 2.4 Demonstrations of the VIV-TENG

Different applications of the VIV-TENG are shown in this subsection. The VIV-TENG is fixed in the frame by four springs. On top of the frame, a wind vane is installed to ensure the VIV-TENG can tune itself with the wind direction. On the bottom of the frame, a circular turntable is installed to enable 360° rotation as shown in Fig. 5(a).

An outdoor experiment is performed to demonstrate the performance of the VIV-TENG under uniform wind conditions. The VIV-TENG can be induced to vibrate in ambient wind speed environment with naturally fluctuating wind speed and direction. The experiment is conducted on the rooftop of a four-story building (20 m height). Firstly, we measure the wind speed every hour using an anemometer (Benetech, GM8903). Despite significant fluctuations in the direction and speed, the average speed of 3.2 m/s is obtained. As shown in Movie ESM3, the VIV-TENG is induced to vibrate at this speed therefore providing the electrical output signals. A circuit is designed for signifying the wind direction, which is presented in Fig. 5(b). When the wind flows from the east direction, the VIV-TENG rotate to the corresponding direction by the wind vane, see Fig. 5(c). There is a rotating switch at the bottom of the turntable, which connects the TENG and the LM 3588 I/O interface 1. The corresponding switch is connected, and an electrical signal is transferred from I/O interface 1 to I/O interface 2. The I/O interface 2 outputs a high level, the direction indicator is activated by this signal. Therefore, the real-time wind direction can be indicated by the VIV-TENG. Figure 5(c) and Movie ESM4 demonstrate that the VIV-TENG can be used to harvest wind energy at naturally environment in which the wind direction varies all the time. As exhibited in Fig. S5, the VIV-TENG does not change significantly under different wind directions. As shown in Fig. 5(d) and Movie ESM5, 200+ LEDs light bulbs can be lit by the VIV-TENG. It is also shown that the VIV-TENG can power commercial electronic sensors without additional battery. As shown in Fig. S6 in the ESM, the voltage of a 100 μF capacitor increases from about 0 V to 3 V in 300 seconds. The thermometer is powered by the capacitor for about 5 seconds as shown in Fig. 5(e) and Movie ESM6. In general, the demonstration experiments show that the VIV-TENG can harvest wind energy in ambient environment and become a power source for the micro electronic devices.

## 3 Conclusion

This study has developed a VIV-TENG of dimensions 150 mm × 30 mm × 30 mm for harvesting wind energy. The performance tests were conducted in a wind tunnel. It was found that the VIV-TENG can be induced to vibrate when the non-dimensional velocity $U^*$ exceeds 7.02 or presently the wind speed $U$> 1.5 m/s. The VIV-TENG has the synchronization range of $U^*$ = 7.02–58.05 (i.e., $U$ = 1.5–12.4 m/s) for harvesting wind energy. This dimensionless range may also apply for large-scale generators. Moreover, by increasing the number of PTFE balls, the output performance of the VIV-TENG becomes better under a constant mass ratio. In addition, the VIV-TENG yields a stable

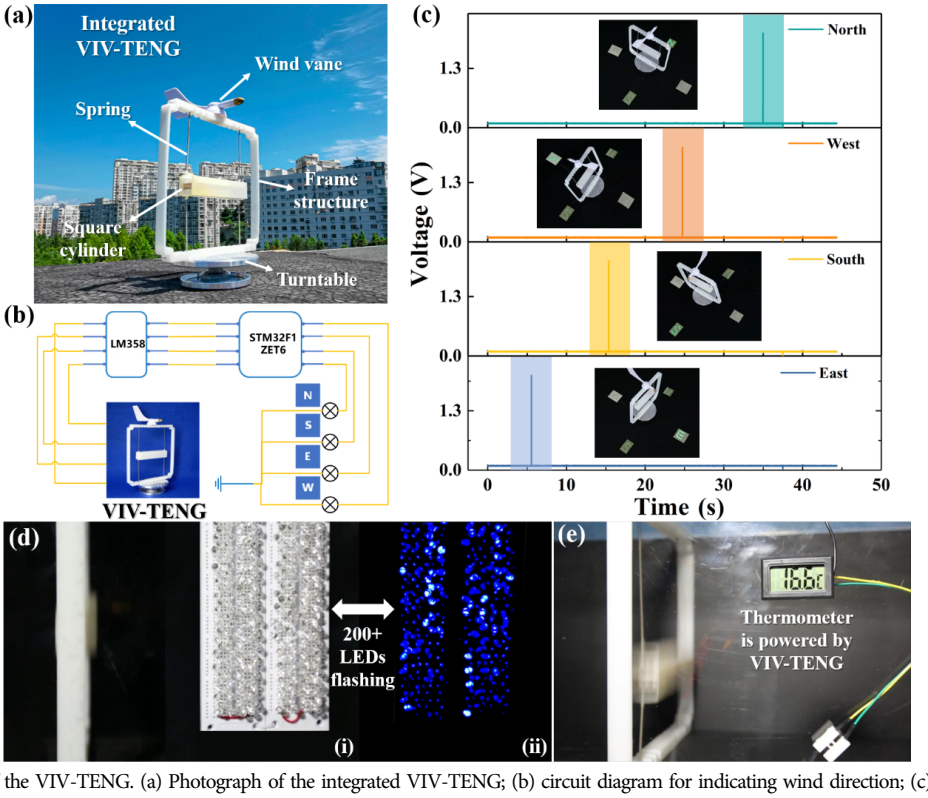


**Figure 5** Application of the VIV-TENG. (a) Photograph of the integrated VIV-TENG; (b) circuit diagram for indicating wind direction; (c) corresponding electric signal of the VIV-TENG for indicating wind direction; (d) 200+ LED light bulbs are lit by the VIV-TENG; (e) a thermometer powered by VIV-TENG.

output performance in the synchronization range. The VIV-TENG with mass ratio $m^*$ = 308.57 can deliver a maximum output power of about 1.7 mW under the matched loading resistance of 200 MΩ with the corresponding peak value of 62.2 W/m$^3$. The VIV-TENG is capable of harvesting wind energy from arbitrary direction by integrating a wind vane. Meanwhile, the fully packaged VIV-TENG has water proof characteristics, which makes it possible to work practically. In sum, this study provides a novel vortex-induced vibration type wind energy harvester.

## 4 Experimental section

### 4.1 Manufacture of the VIV-TENG

The fabrication of the VIV-TENG is shown in Fig. 1(aii). PLA material is used to print the frame structure and internal power generation unit. The internal power generation unit adopts a honeycomb structure to accommodate more PTFE balls in the limited space, and its dimension is 130 mm (length) × 8 mm (height) × 26 mm (width). The internal power generation unit of the VIV-TENG is fixed inside the square cylinder. There are two caps at the end of the square cylinder, which can ensure the internal power generation unit is isolated from the outside atmosphere when the VIV-TENG works. The internal power generation unit is also sealed by the waterproof PTFE tape. All these operations can ensure the triboelectric layer is isolated from the air. The distance between two electrodes is determined by the height of the honeycomb structure. The honeycomb structure is printed by the 3D printer. The distance between the two electrodes can be adjusted by setting the height of the 3D printing device. The gaps between the electrodes and the honeycomb structure are sealed by tape for waterproof. The VIV-TENG is installed on a circular turntable, and the VIV-TENG has ability to adapt wind direction by integrating a wind vane as depicted in Fig. 5(a). Once wind flows around the square cylinder, it can vibrate up and down, thus producing alternating electric signals.

### 4.2 Wind tunnel tests and electrical output measurements

The open loop wind tunnel used in the experiment has a testing section, which is 1.0 m long, 0.25 m wide and 0.25 m high. The rotating speed of blower is controlled by an inverter, then varies the wind speed. The visualization of fluid interaction with the VIV-TENG is realized by the smoke flow method. The vortex shedding is captured by the high-speed camera (FATCAM Mini UX50). A Keithley 6514 system electrometer is used to measure the output performance of the VIV-TENG.

## Acknowledgements

The work was supported by the National Natural Science Foundation of China (Nos. 51879022, 51979045, 52101400, 52101382, and 52101345), China Scholarship Council (CSC No. 202006570022), the Fundamental Research Funds for the Central Universities, China (Nos. 3132019330, 3132021340), Science and Technology Innovation Foundation of Dalian (No. 2021JJ12GX028), Innovation Group Project of Southern Marine Science and Engineering Guangdong Laboratory (Zhuhai) (No. 311021013).

**Electronic Supplementary Material**: Supplementary material (additional output performance) is available in the online version of this article at https://doi.org/10.1007/s12274-021-3968-9.

## References

[1] Wang, J. L.; Zhao, G. F.; Zhang, M.; Zhang, Z. E. Efficient study of a coarse structure number on the bluff body during the harvesting of wind energy. *Energy Sour. A* **2018**, *40*, 1788–1797.

[2] Scrosati, B. Power sources for portable electronics and hybrid cars: Lithium batteries and fuel cells. *Chem. Rec.* **2005**, *5*, 286–297.

[3] Chen, Y.; Mu, X. J.; Wang, T.; Ren, W. W.; Yang, Y.; Wang, Z. L.; Sun, C. L.; Gu, A. Y. Flutter phenomenon in flow driven energy harvester-a unified theoretical model for "stiff" and "flexible" materials. *Sci. Rep.* **2016**, *6*, 35180.

[4] Jiang, D. Y.; Xu, M. Y.; Dong, M.; Guo, F.; Liu, X. H.; Chen, G. J.; Wang, Z. L. Water-solid triboelectric nanogenerators: An alternative means for harvesting hydropower. *Renew. Sust. Energy Rev.* **2019**, *115*, 109366.

[5] Maitra, A.; Bera, R.; Halder, L.; Bera, A.; Paria, S.; Karan, S. K.; Si, S. K.; De, A.; Ojha, S.; Khatua, B. B. Photovoltaic and triboelectrification empowered light-weight flexible self-charging asymmetric supercapacitor cell for self-powered multifunctional electronics. *Renew. Sust. Energy Rev.* **2021**, *151*, 111595.

[6] Wu, M.; Gao, Z.; Yao, K.; Hou, S.; Liu, Y.; Li, D.; He, J.; Huang, X.; Song, E.; Yu, J. et al. Thin, soft, skin-integrated foam-based triboelectric nanogenerators for tactile sensing and energy harvesting. *Mater. Today Energy* **2021**, *20*, 100657.

[7] Yang, Y. F.; Yu, X.; Meng, L. X.; Li, X.; Xu, Y. H.; Cheng, T. H.; Liu, S. M.; Wang, Z. L. Triboelectric nanogenerator with double rocker structure design for ultra-low-frequency wave full-stroke energy harvesting. *Extreme Mech. Lett.* **2021**, *46*, 101338.

[8] Liu, L.; Shi, Q. F.; Lee, C. A hybridized electromagnetic-triboelectric nanogenerator designed for scavenging biomechanical energy in human balance control. *Nano Res.* **2021**, *14*, 4227–4235.

[9] Pan, L.; Wang, J. Y.; Wang, P. H.; Gao, R. J.; Wang, Y. C.; Zhang, X. W.; Zou, J. J.; Wang, Z. L. Liquid-FEP-based U-tube triboelectric nanogenerator for harvesting water-wave energy. *Nano Res.* **2018**, *11*, 4062–4073.

[10] Quan, T.; Yang, Y. Fully enclosed hybrid electromagnetic-triboelectric nanogenerator to scavenge vibrational energy. *Nano Res.* **2016**, *9*, 2226–2233.

[11] Li, Y. H.; Zhang, Q.; Liu, Y.; Zhang, P. L.; Ren, C.; Zhang, H. D.; Cai, H.; Ding, G. F.; Yang, Z. Q.; Zhang, C. Regulation of nanocrystals structure for high-performance magnetic triboelectric nanogenerator. *Nano Energy* **2021**, *89*, 106390.

[12] Liu, S.; Li, P.; Yang, Y. R. On the design of an electromagnetic aeroelastic energy harvester from nonlinear flutter. *Meccanica* **2018**, *53*, 2807–2831.

[13] Datta, R.; Ranganathan, V. T. Direct power control of grid-connected wound rotor induction machine without rotor position sensors. *IEEE Trans. Power Electr.* **2002**, *16*, 390–399.

[14] Zheng, H. W.; Zi, Y. L.; He, X.; Guo, H. Y.; Lai, Y. C.; Wang, J.; Zhang, S. L.; Wu, C. S.; Cheng, G.; Wang, Z. L. Concurrent harvesting of ambient energy by hybrid nanogenerators for wearable self-powered systems and active remote sensing. *ACS Appl. Mater. Interfaces* **2018**, *10*, 14708–14715.

[15] Su, Y. J.; Xie, G. Z.; Xie, T.; Zhang, H. L.; Ye, Z. B.; Jing, Q. S.; Tai, H. L.; Du, X. S.; Jiang, Y. D. Wind energy harvesting and self-powered flow rate sensor enabled by contact electrification. *J. Phys. D Appl. Phys.* **2016**, *49*, 215601.

[16] Phan, H.; Shin, D. M.; Jeon, S. H.; Kang, T. Y.; Han, P.; Kim, G. H.; Kim, H. K.; Kim, K.; Hwang, Y. H.; Hong, S. W. Aerodynamic and aeroelastic flutters driven triboelectric nanogenerators for harvesting broadband airflow energy. *Nano Energy* **2017**, *33*, 476–484.

[17] Liu, L.; Guo, X. E.; Lee, C. Promoting smart cities into the 5G era with multi-field Internet of Things (IoT) applications powered with advanced mechanical energy harvesters. *Nano Energy* **2021**, *88*, 106304.

[18] Wang, Y.; Wang, J. Y.; Xiao, X.; Wang, S. Y.; Kien, P. T.; Dong, J. L.; Mi, J. C.; Pan, X. X.; Wang, H. F.; Xu, M. Y. Multi-functional wind barrier based on triboelectric nanogenerator for power generation, self-powered wind speed sensing and highly efficient windshield. *Nano Energy* **2020**, *73*, 104736.

[19] Sun, W. P.; Ding, Z.; Qin, Z. Y.; Chu, F. L.; Han, Q. K. Wind energy harvesting based on fluttering double-flag type triboelectric nanogenerators. *Nano Energy* **2020**, *70*, 104526.

[20] Xu, M. Y.; Wang, Y. C.; Zhang, S. L.; Ding, W. B.; Cheng, J.; He, X.; Zhang, P.; Wang, Z. J.; Pan, X. X.; Wang, Z. L. An aeroelastic flutter based triboelectric nanogenerator as a self-powered active wind speed sensor in harsh environment. *Extreme Mech. Lett.* **2017**, *15*, 122–129.

[21] Zhang, C. G.; Liu, Y. B.; Zhang, B. F.; Yang, O.; Yuan, W.; He, L. X.; Wei, X. L.; Wang, J.; Wang, Z. L. Harvesting wind energy by a triboelectric nanogenerator for an intelligent high-speed train system. *ACS Energy Lett.* **2021**, *6*, 1490–1499.

[22] Chen, P. F.; An, J.; Shu, S.; Cheng, R. W.; Nie, J. H.; Jiang, T.; Wang, Z. L. Super-durable, low-wear, and high-performance fur-brush triboelectric nanogenerator for wind and water energy harvesting for smart agriculture. *Adv. Energy Mater.* **2021**, *11*, 2003066.

[23] Shi, Q. F.; Zhang, Z. X.; He, T. Y. Y.; Sun, Z. D.; Wang, B. J.; Feng, Y. Q.; Shan, X. C.; Salam, B.; Lee, C. Deep learning enabled smart mats as a scalable floor monitoring system. *Nat. Commun.* **2020**, *11*, 4609.

[24] Bae, J.; Lee, J.; Kim, S.; Ha, J.; Lee, B. S.; Park, Y.; Choong, C.; Kim, J. B.; Wang, Z. L.; Kim, H. Y. et al. Flutter-driven triboelectrification for harvesting wind energy. *Nat. Commun.* **2014**, *5*, 4929.

[25] Zhang, Y.; Fu, S. C.; Chan, K. C.; Shin, D. M.; Chao, C. Y. H. Boosting power output of flutter-driven triboelectric nanogenerator by flexible flagpole. *Nano Energy* **2021**, *88*, 106284.

[26] Hu, J.; Pu, X. J.; Yang, H. M.; Zeng, Q. X.; Tang, Q.; Zhang, D. Z.; Hu, C. G.; Xi, Y. A flutter-effect-based triboelectric nanogenerator for breeze energy collection from arbitrary directions and self-powered wind speed sensor. *Nano Res.* **2019**, *12*, 3018–3023.

[27] Perez, M.; Boisseau, S.; Gasnier, P.; Willemin, J.; Reboud, J. L. An electret-based aeroelastic flutter energy harvester. *Smart Mater. Struct.* **2015**, *24*, 035004.

[28] Xie, Y. N.; Wang, S. H.; Lin, L.; Jing, Q. S.; Lin, Z. H.; Niu, S. M.; Wu, Z. Y.; Wang, Z. L. Rotary triboelectric nanogenerator based on a hybridized mechanism for harvesting wind energy. *ACS Nano* **2013**, *7*, 7119–7125.

[29] Wang, Y. Q.; Yu, X.; Yin, M. F.; Wang, J. L.; Gao, Q.; Yu, Y.; Cheng, T. H.; Wang, Z. L. Gravity triboelectric nanogenerator for the steady harvesting of natural wind energy. *Nano Energy* **2021**, *82*, 105740.

[30] Ren, X. H.; Fan, H. Q.; Wang, C.; Ma, J. W.; Li, H.; Zhang, M. C.; Lei, S. H.; Wang, W. J. Wind energy harvester based on coaxial rotatory freestanding triboelectric nanogenerators for self-powered water splitting. *Nano Energy* **2018**, *50*, 562–570.

[31] Yong, S.; Wang, J. Y.; Yang, L. J.; Wang, H. Q.; Luo, H.; Liao, R. J.; Wang, Z. L. Auto-switching self-powered system for efficient broad-band wind energy harvesting based on dual-rotation shaft triboelectric nanogenerator. *Adv. Energy Mater.* **2021**, *11*, 2101194.

[32] Williamson, C. H. K.; Govardhan, R. Vortex-induced vibrations. *Annu. Rev. Fluid Mech.* **2004**, *36*, 413–455.

[33] Blevins, R. D. *Flow-Induced Vibrations*; Van Nostrand Reinhold: New York, 1990; pp 377.

[34] Xiao, X.; Zhang, X. Q.; Wang, S. Y.; Ouyang, H.; Chen, P. F.; Song, L. G.; Yuan, H. C.; Ji, Y. L.; Wang, P. H.; Li, Z. et al. Honeycomb structure inspired triboelectric nanogenerator for highly effective vibration energy harvesting and self-powered engine condition monitoring. *Adv. Energy Mater.* **2019**, *9*, 1902460.

[35] Du, T. L.; Zuo, X. S.; Dong, F. Y.; Li, S. Q.; Mtui, A. E.; Zou, Y. J.; Zhang, P.; Zhao, J. H.; Zhang, Y. W.; Sun, P. T. et al. A self-powered and highly accurate vibration sensor based on bouncing-ball triboelectric nanogenerator for intelligent ship machinery monitoring. *Micromachines* **2021**, *12*, 218.

[36] Shao, Z.; Zhou, T. M.; Zhu, H. J.; Zang, Z. P.; Zhao, W. H. Amplitude enhancement of flow-induced vibration for energy harnessing. In *Proceedings of the 6th International Conference on Renewable Energy Technologies*, Perth, Australia, 2020, pp 01005.

[37] Niu, S. M.; Liu, Y.; Chen, X. Y.; Wang, S. H.; Zhou, Y. S.; Lin, L.; Xie, Y. N.; Wang, Z. L. Theory of freestanding triboelectric-layer-based nanogenerators. *Nano Energy* **2015**, *12*, 760–774.

[38] Bernitsas, M. M.; Raghavan, K.; Ben-Simon, Y.; Garcia, E. M. H. VIVACE (Vortex induced vibration aquatic clean energy): A new concept in generation of clean and renewable energy from fluid flow. *J. Offshore Mech. Arct. Eng.* **2008**, *130*, 041101.

[39] Khalak, A.; Williamson, C. H. K. Motions, forces and mode transitions in vortex-induced vibrations at low mass-damping. *J. Fluids Struct.* **1999**, *13*, 813–851.

[40] Govardhan, R.; Williamson, C. H. K. Modes of vortex formation and frequency response of a freely vibrating cylinder. *J. Fluid Mech.* **2000**, *420*, 85–130.

[41] Feng, C. C. The measurement of vortex induced effects in flow past stationary and oscillating circular and d-section cylinders. Master Degree Thesis, University of British Columbia, Vancouver, 1968.
[42] Sarpkaya, T. A critical review of the intrinsic nature of vortex-induced vibrations. *J. Fluids Struct.* **2004**, *19*, 389–447.
[43] Bernitsas, M. M.; Ben-Simon, Y.; Raghavan, K.; Garcia, E. M. H. The VIVACE converter: Model tests at high damping and reynolds number around $10^5$. *J. Offshore Mech. Arct. Eng.* **2006**, *131*, 011102.
[44] Zhou, T.; Razali, S. F. M.; Hao, Z.; Cheng, L. On the study of vortex-induced vibration of a cylinder with helical strakes. *J. Fluids Struct.* **2011**, *27*, 903–917.
[45] Modir, A.; Goudarzi, N. Experimental investigation of Reynolds number and spring stiffness effects on vortex induced vibrations of a rigid circular cylinder. *Eur. J. Mech. B Fluids* **2019**, *74*, 34–40.
[46] McCarty, L. S.; Whitesides, G. M. Electrostatic charging due to separation of ions at interfaces: Contact electrification of ionic electrets. *Angew. Chem., Int. Ed.* **2008**, *47*, 2188–2207.